

Action Quality Assessment via Hierarchical Pose-guided Multi-stage Contrastive Regression

Mengshi Qi, *Member, IEEE*, Hao Ye, Jiaxuan Peng, Huadong Ma, *Fellow, IEEE*

Abstract—Action Quality Assessment (AQA), which aims at automatic and fair evaluation of athletic performance, has gained increasing attention in recent years. However, athletes are often in rapid movement and the corresponding visual appearance variances are subtle, making it challenging to capture fine-grained pose differences and leading to poor estimation performance. Furthermore, most common AQA tasks, such as diving in sports, are usually divided into multiple sub-actions, each of which contains different durations. However, existing methods focus on segmenting the video into fixed frames, which disrupts the temporal continuity of sub-actions resulting in unavoidable prediction errors. To address these challenges, we propose a novel action quality assessment method through hierarchically pose-guided multi-stage contrastive regression. Firstly, we introduce a multi-scale dynamic visual-skeleton encoder to capture fine-grained spatio-temporal visual and skeletal features. Then, a procedure segmentation network is introduced to separate different sub-actions and obtain segmented features. Afterwards, the segmented visual and skeletal features are both fed into a multi-modal fusion module as physics structural priors, to guide the model in learning refined activity similarities and variances. Finally, a multi-stage contrastive learning regression approach is employed to learn discriminative representations and output prediction results. In addition, we introduce a newly-annotated FineDiving-Pose Dataset to improve the current low-quality human pose labels. In experiments, the results on FineDiving and MTL-AQA datasets demonstrate the effectiveness and superiority of our proposed approach. Our source code and dataset are available at <https://github.com/Lumos0507/HP-MCoRe>.

Index Terms—Action Quality Assessment, Contrastive Regression, Multi-stage Segmentation, Human Pose Estimation

I. INTRODUCTION

ACTION quality assessment (AQA) [1]–[7] has garnered significant attention within the computer vision community, aiming to assess the quality of action execution. In practical applications, AQA plays a crucial role across various domains, such as automating evaluations in sports (e.g., gymnastics or diving) [2], [8]–[10], providing corrective guidance in rehabilitation training [8], [11]–[13], and obtaining performance feedback in skill learning. Unlike daily life videos, action videos in the AQA task are characterized by sequential processes and domain-specific execution standards, necessitating a deep understanding of actions and an accurate analysis of fine-grained sub-action features. These include subtle differences in limb and torso movements as well as

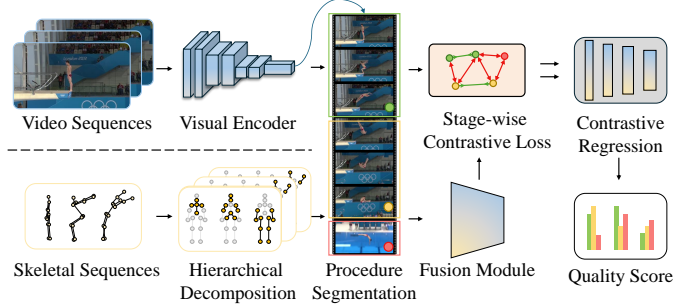


Fig. 1. Illustration of our proposed framework for AQA. The framework integrates both human visual and hierarchical skeletal information to capture fine-grained features and physical priors for the high-quality action assessment. Additionally, we introduce a procedure segmentation module that dynamically models the sub-action sequences. Subsequently, we fuse the skeletal and visual features to derive spatiotemporal features. Finally, we propose a contrastive learning-based regression approach to enhance the evaluation accuracy.

variations in action durations. Additionally, performers in AQA tasks frequently exhibit rapid motion, which often leads to blurred frames, further complicating the assessment process.

Most existing approaches [1]–[5] treat the AQA task as either a regression problem or a pairwise comparison regression problem, typically focusing on coarse-grained action features and utilizing holistic video representations extracted from videos. However, as previously discussed, coarse-grained features are not adequately supportive of high-quality evaluation, as holistic video representations struggle to capture the intricate variations between different sub-actions within a complete action sequence. Although impressive performance has been achieved by using powerful visual backbones to extract video features in recent works [14]–[19], these methods still face significant challenges. Specifically, performers, particularly professional athletes in sports videos, often exhibit rapid motion, accompanied by complex limb coordination and bending, resulting in frequently blurred video frames. This poses challenges for backbones to accurately capture fine-grained pose and physical structure differences among various athletes performing the same action.

Additionally, sports such as diving and gymnastics often comprise multiple discrete phases within a single performance [14], exemplified by the *take-off*, *flight*, and *entry* phases in a diving maneuver. Judges predominantly focus on the nuanced distinctions in athletes’ executions across each sub-action, encompassing the number of flips, twists, and the posture during flight. Existing methods [14], [20] typically segment input videos into fixed-frame clips and employ specific network structures to process these clips in a global manner. However, such approaches disrupt the temporal continuity of sub-actions,

This work is partly supported by the Funds for the NSFC Project under Grant 62202063, Beijing Natural Science Foundation (L243027). (Corresponding author: Mengshi Qi (email: qms@bupt.edu.cn))

M. Qi, H. Ye, J. Peng and H. Ma are with State Key Laboratory of Networking and Switching Technology, Beijing University of Posts and Telecommunications, China.

as the durations of phases often vary across different action categories. Identifying and segmenting each phase within an action sequence is believed to enable more precise analysis and conclusive evaluation [1], [2], [21]. Therefore, it is crucial to dynamically segment the videos. However, clips corresponding to different sub-actions often share similar visual backgrounds and features, which presents significant challenges for dynamic action segmentation.

As illustrated in Figure 1, we propose a hierarchically pose-guided multi-stage action quality assessment framework to address the aforementioned challenges. This framework processes action videos and corresponding skeleton sequences as inputs. Compared to blurred video frames, the skeleton sequences of performers offer precise spatial coordinates and motion trajectories, thereby providing more fine-grained sub-action features [22]–[26]. The proposed framework primarily consists of two branches: a static branch and a dynamic branch. The static branch utilizes a static visual encoder to process video frames, aiming to retain more contextual details and enhance action representation. The proposed dynamic branch, comprising a dynamic visual encoder and a hierarchical skeletal encoder, captures fine-grained spatiotemporal differences and physical priors to guide feature fusion through a multi-modal fusion module. During this process, the procedure segmentation module distinguishes different stages of sub-actions and segments all features accordingly. Finally, the multi-stage features from both the static and dynamic branches are passed through the stage contrastive regression module to obtain discriminative features, leading to an understanding of differences in athlete actions across different videos. To optimize the model’s understanding of different sub-actions, we design a stage contrastive loss to perform unsupervised training and learn the differences between sub-actions.

It should be noted that this paper is an extension of our conference paper [19]. Compared to the preliminary version, we leverage an additional skeletal modality to obtain hierarchical human pose features. Given the limitations in existing datasets characterized by the poor quality or absence of skeletal labels, we also present a newly-annotated *FineDiving-Pose Dataset* with refined pose labels, which are collected through a combination of manual annotation and automatic generation to boost the related field further. Furthermore, we propose a multi-modal fusion module to integrate visual features and skeletal features and add a static branch to capture human static features. Additionally, we perform additional experiments on another public benchmark dataset (MTL-AQA [6]), and we conduct more detailed ablation experiments and then present more qualitative results to demonstrate the effectiveness of each component within the framework proposed in this paper.

The contributions of this paper are summarized as follows:

- We propose a hierarchical pose-guided AQA framework, which introduces the combination of static and dynamic visual branches to decompose pose information and guide the fusion of pose features with dynamic video features for capturing fine-grained spatiotemporal features.
- We develop a procedure segmentation network, which divides the input sequences into multiple stages to learn broader contextual information, along with a stage

contrastive learning regression module to enhance the model’s ability to learn differences between sub-actions.

- We introduce a newly annotated *FineDiving-Pose Dataset* to boost the AQA research further, which contains 12,722 human annotated pose labels and 288,000 automatically-annotated pose labels by our proposed annotated pipeline.
- We conduct extensive experiments on two mainstream datasets, *FineDiving* [14] and *MTL-AQA* [6], to evaluate our method, demonstrating that our approach outperforms state-of-the-art methods.

II. RELATED WORK

AQA. Currently, the AQA task mainly follows two types of formulations: *regression* and *pairwise ranking*. *Regression-based* approaches [3], [4], [6], [14], [16], [27] are widely applied in sports such as diving, skiing, and synchronized swimming. Pirsiavash et al. [3] pioneered the using of regression models for human action quality assessment, predicting action scores directly from video features. Parmar et al. [6] proposed a multi-task clip-level scoring method by utilizing spatiotemporal action features. Tang et al. [4] proposed an uncertainty-aware score distribution learning framework, thereby addressing the uncertainties arising from subjective evaluations. Zeng et al. [27] proposed a hybrid method that integrates static and dynamic action features, accounting for the contributions of different temporal segments. Xu et al. [14] proposed a procedure-aware representation by designing a temporal segmentation attention module. Zhou et al. [16] proposed a hierarchical graph convolutional network (GCN) to refine semantic features, and aggregate dependencies for analyzing action procedures and motion units. While *Pairwise ranking-based* approaches [28]–[33] tackle the challenge of distinguishing subtle differences between actions in similar contexts, by evaluating the score of a given video relative to other videos through pairwise comparisons. Yu et al. [2] were the first to propose a pairwise ranking-based approach for diving to learn relative scores. Li et al. [21] further enhanced the model’s ability to capture subtle score differences by incorporating Pairwise Contrastive Learning Network. Similarly, An et al. [19] proposed a multi-stage contrastive regression framework to efficiently extract spatiotemporal features for AQA. These methods primarily focus on evaluating entire video sequences either within the same video or across different videos. In contrast, our approach divides video sequences into different phases and then used the fused visual-skeletal representation, enabling fine-grained contrastive learning of motion differences at each stage.

Multimodal Learning in AQA. Different modalities are leveraged in AQA, which can be divided into *vision-based* methods and *skeleton-based* methods. *Vision-based* approaches typically leverage powerful backbone architectures, such as C3D [34] and I3D [35]. Parmar et al. [36] were the first to utilize a segment-level C3D network [34] to extract features, with an LSTM network [37] to capture temporal relationships between video segments. Building on this, Li et al. [28] introduced a spatial attention network, which involved segmenting the video, performing random sparse sampling, and using RGB

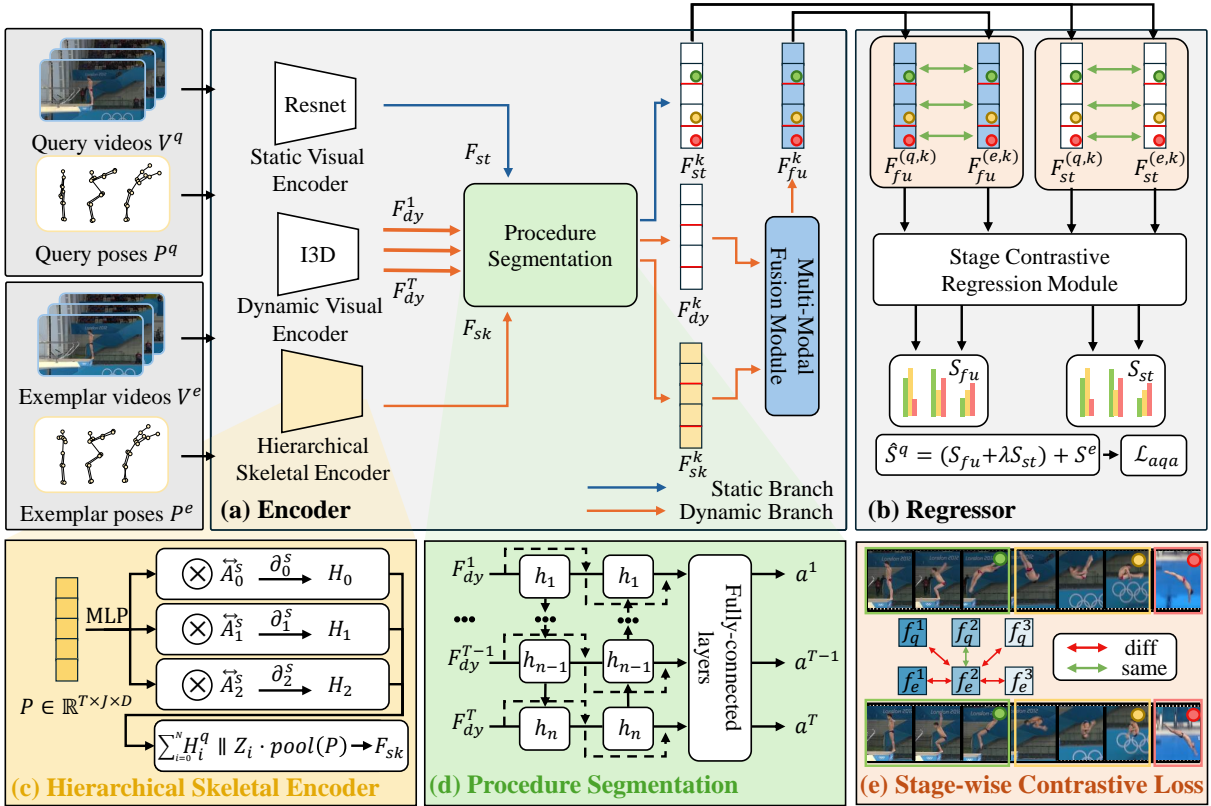


Fig. 2. Overview of our proposed hierarchical pose-guided multi-stage action quality assessment framework. **Encoder:** The framework takes query pairs V^q, P^q as input for testing, while exemplar pairs V^e, P^e are selected from an existing dataset. The dynamic visual encoder and the (c) **hierarchical skeletal encoder** capture the spatiotemporal visual and pose features F_{dy} and F_{sk} . The static visual encoder captures static human features F_{st} . The (d) **procedure segmentation network** segments these features into \mathbb{K} stages, resulting in F_{dy}^k, F_{sk}^k and F_{st}^k . The (e) **stage-wise contrastive loss** is applied to enhance segmentation accuracy. The multi-stage features of F_{dy}^k and F_{sk}^k are input into the multi-modal fusion module to obtain the fused features F_{fu}^k . **Regressor:** The inputs are fused dynamic features and static features of the k -th segmentation, denoted as $F_{fu}^{(q,k)}, F_{sk}^{(q,k)}, F_{fu}^{(e,k)}$ and $F_{st}^{(e,k)}$. The static features and fused features are fed into the stage contrastive regression module separately to obtain the relative scores S_{fu} and S_{st} . Finally, a confidence value λ is applied, and the exemplar score S_e is added to produce the predicted score \hat{S}^q .

images and optical flow to extract informative features. Wang et al. [38] subsequently integrated a single-object tracker to enhance the distinction between foreground and background in feature maps. *Skeleton-based* approaches [1], [24], [26], [39]–[41] focus on leveraging detailed human pose information to capture the positions and movements of individual body parts. Early approaches [39], [40] relied on specialized equipment to capture athlete poses, which limited their applicability to real-world scenarios. However, recent advances in pose estimation have rendered these approaches more practical. Pan et al. [1] proposed to learn interactions between pose joints, demonstrating that fine-grained pose information can enhance model performance. Nekoui et al. [26] employed a joint coordination evaluator in combination with multi-scale convolution to capture temporal dependencies, while okamoto et al. [41] conducted a detailed analysis of athletes’ actions using a neuro-symbolic approach. In our work, we propose a new hierarchical pose-guided action quality assessment method, which decomposes athlete skeletal poses into several meaningful sub-sets to highlight diverse motion features, thereby enhancing AQA performance.

III. PROPOSED APPROACH

A. Overview

Our proposed framework is illustrated in Figure 2. Firstly, a multi-scale visual-skeletal encoder is introduced to capture fine-grained spatiotemporal and static features from visual frames and skeletal pose. Next, the procedure segmentation module is designed to distinguish different temporal stages for both dynamic and static features. By comparing the action features across different stages, stage-level features are obtained. The segmented dynamic visual features and skeletal features are then processed through the multi-modal fusion module. Finally, a multi-stage contrastive learning regression method is utilized to learn discriminative representations to estimate the quality score.

Problem Formulation. Given a pair of query video V^q and exemplar video V^e , along with their respective skeletal sequences P^q and P^e , the object is to predict quality score \hat{S}^q of V^q based on the quality score S^e of V^e , which is formulated as the following:

$$\hat{S}^q = \mathcal{F}(V^q, P^q, V^e, P^e | \Theta) + S^e, \quad (1)$$

where $\mathcal{F}(\cdot | \Theta)$ represents the overall network architecture, with Θ denoting the parameters of the model, $V \in \mathbb{R}^{T \times H \times W \times C}$

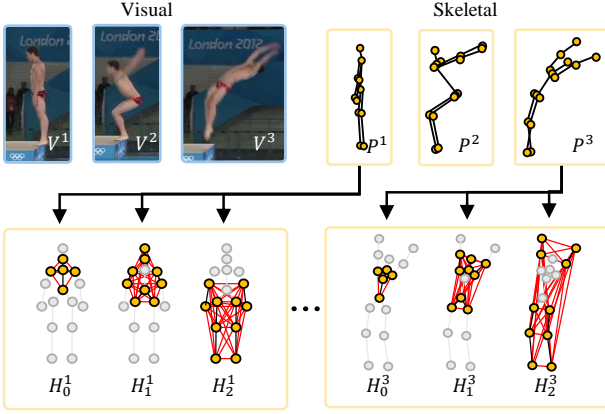


Fig. 3. The illustration of the hierarchical pose encoding. We decompose the human pose into three levels using a graph convolutional network. The first level focuses on the torso, capturing the correctness of the torso rotation. The second level focuses on the inner parts of the limbs, capturing transitions between actions. The third level targets the outer parts of the limbs, capturing the coordination of the athlete’s body movements.

and $P \in \mathbb{R}^{T \times J \times D_c}$, where T, H, W, C denote the number of frames, height, width, and the number of channels respectively, and J, D_c refer to the number of human joints and the coordinate dimension of joints. This regression problem aims to obtain the final score by predicting the relative score difference between the query video and the exemplar video.

B. Multi-Scale Visual-Skeletal Encoder

As illustrated in Figure 2, we introduce the multi-scale visual-skeletal encoder that consists of three components: static visual encoder, dynamic visual encoder for extracting visual features, and the hierarchical skeletal encoder for capturing human pose features.

Static Visual Encoder: This component is designed to capture human static features and enhance the action representation at each temporal step. We adopt ResNet-50 [42] as the backbone, which places more emphasis on appearance information from individual RGB frames, compared to I3D [35]. The encoder consists of a ResNet-50 model denoted as \mathcal{R} and a multi-branch downsampling module $Down_{mul}$. Specifically, the ResNet model is primarily adopted to extract high-level global features from the input video, while the multi-branch downsampling module, consisting of a convolutional layer and three downsampling layers, captures local detailed information at different spatial scales. The static feature F_{st} can be obtained from this module as follows:

$$F_{st} = Down_{mul}(\mathcal{R}(V)), \quad (2)$$

where V represents query or exemplar video frames.

Dynamic Visual Encoder: This component is responsible for extracting spatiotemporal features and complex dynamic information from the video sequence, such as the sequence of an action from preparation to take-off. We adopt I3D [35] as the backbone network, denoted as \mathcal{I} , to encode the video input. To expand the temporal dimension’s receptive field, mixed convolution layers are introduced before the max-pooling layer. Specifically, the query video V^q is fed into

the backbone network \mathcal{I} , followed by convolution operations along the temporal axis to dilate the temporal dimension of $\mathcal{I}(V^q)$, and a max-pooling operation along the spatial axis, which is formulated as follows:

$$F_{dy}^q = \maxpool(Conv_{mix}(\mathcal{I}(V^q))), \quad (3)$$

where $Conv_{mix}$ represents the mixed convolution layers, consisting of three layers, and $F_{dy}^q \in \mathbb{R}^{T \times D}$ is the final visual spatiotemporal feature. Similarly, the exemplar video V^e also obtains the corresponding F_{dy}^e .

Hierarchical Skeletal Encoder: Taking into account the kinematic principles and trajectory patterns, we observe that distant joints (e.g., hands and feet) execute both substantially and refined actions, while central joints (e.g., the torso) exhibit minimal actions yet are highly responsive to the overall body displacement. In light of these observations, we endeavor to decompose the full range of skeletal joints into three distinct semantic levels, differentiated by the amplitude and directionality of joint movements, as depicted in Figure 3.

To be specific, the lowest level H_0 encapsulates the motion of the torso, which is indicative of the body’s spatial dynamics within pose sequences. The highest level H_2 , characterized by the highest motion amplitude, captures the intricate and rich movements, encompassing joints that engage in agile and rapid sub-actions, such as the swift movements of the wrists and ankles observed in twists in straight, pike or tuck positions within diving scenario. The features derived from H_2 are particularly fine-grained, as these motions are the focus of scrutiny during assessment. The intermediate level H_1 serves as a bridge between H_0 and H_2 , tasked with capturing the transitional aspects of sub-actions, exemplified by the changes in the angles of the elbow and knee from the *take-off* to the *flight* in diving scenario.

As illustrated in Figure 2 (c), the hierarchical skeletal encoder enhances feature capture capabilities at different levels through four parallel branches, including three graph convolutions. Each graph convolution corresponds to a specific skeletal level (e.g., H_0). For each level, we perform GCN operations to extract feature and concatenate the features of each level, which is formulated as

$$H_i^q = \parallel_{s \in S} \{ \overleftrightarrow{\mathbf{A}}_i^s \text{MLP}(P^q) \partial_i^s \}, \quad (4)$$

where $\overleftrightarrow{\mathbf{A}}_i^s \in \mathbb{R}^{N_s \times D \times D}$ denotes the skeletal node adjacency matrix for the i -th layer, and $S = \{s_{id}, s_{cf}, s_{cp}\}$ denotes above-mentioned three pose skeleton subsets, and s_{id}, s_{cf}, s_{cp} indicate identity, centrifugal, and centripetal joint subsets, respectively. $\text{MLP}(\cdot)$ represents one layer MLP with parameters $W \in \mathbb{R}^{D' \times D}$, ∂_i^s is the point-wise convolution operation, \parallel denotes concatenation along with the channel dimension, and $H^q = \{H_0^q, H_1^q, H_2^q\}$.

The three semantic levels defined above are introduced to model kinematic and motion information, but they exist as sparse graphs where the edges represent only physical connections. These edges are inadequate to capture implicit features that are embedded within the relationships among distant joint nodes. Therefore, we expand the human pose graph through connecting all nodes in adjacent levels, with

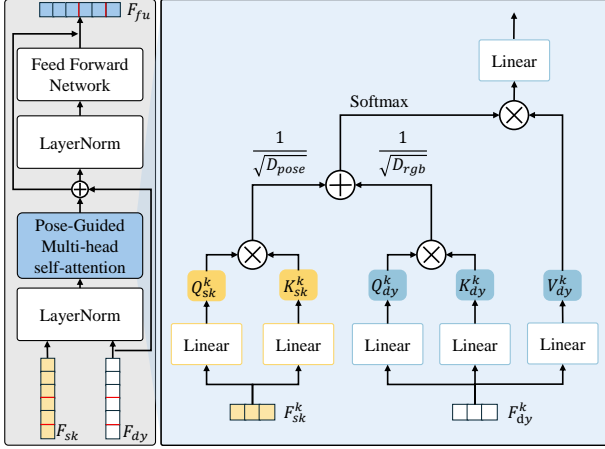


Fig. 4. Illustration of the Multi-modal Fusion Module. We propose a pose-guided attention into such module where the input pose and visual features share the same procedure segmentation information, ensuring consistency in their corresponding spatiotemporal information.

the dual objective of capturing both explicit and implicit features. Specifically, we first apply average pooling to obtain the average feature of each node. Then, the EdgeConv [43] is employed to capture both explicit and implicit features. This operation effectively reflects relationships between physically joint edges in shallow layers and semantically similar edges in deeper layers. The EdgeConv operation can be defined as follows:

$$F_{sk}^q = \sum_{i=1}^N [H_i^q \parallel Z_i \cdot \frac{1}{T} \sum_{t=1}^T \text{MLP}(P^q)], \quad (5)$$

where Z_i is the EdgeConv operation at the i -th layer, N denotes different skeletal semantic levels. The skeletal pose P^q , after passing through the hierarchical skeletal encoder, produces the skeletal feature output $F_{sk}^q \in \mathbb{R}^{T \times J \times D}$. Similarly, P^e can also obtain the skeletal feature output F_{sk}^e .

C. Procedure Segmentation Module

During competition, judges typically focus on the performance of the athlete at different stages of the action [41], assigning an overall score based on the effectiveness of each sub-action. For example, the athlete’s movement can be divided into *take-off*, *flight*, and *entry* in the diving scenario. In our approach, we independently score the actions within each stage to achieve more accurate predictions. To enable the model to distinguish the significant variances between sub-actions, we propose a procedure segmentation network. We assume that the action video can be divided into \mathbb{K} stages, and the goal of the procedure segmentation network is to predict the $\mathbb{K} - 1$ moments where stage transitions occur. To capture long-term temporal dependencies, we propose a procedure segmentation network \mathcal{P} based on the Bidirectional Gated Recurrent Unit (Bi-GRU) [44] followed by a fully connected layer and a softmax operation. Specifically, the dynamic visual feature F_{dy} is input to \mathcal{P} to predict the stage transition labels, which can be expressed as follows:

$$\mathcal{P}(F_{dy}) = [\hat{a}_1, \hat{a}_2, \dots, \hat{a}_T]. \quad (6)$$

Here, \hat{a}_i denotes the predicted label of the i -th frame. If the predicted labels of the i -th frame and the $(i - 1)$ -th frame are identical, it indicates that both frames belong to the same sub-action stage, and we set $\hat{a}_i = 0$. Conversely, if the predicted labels differ, it signifies that the i -th frame marks the transition to the next sub-action stage, and set $\hat{a}_i = 1$.

Next, we identify the frames with the highest probability as the prediction of stage transitions. The per-frame classification task is optimized using the cross-entropy loss. The loss function \mathcal{L}_{ce} calculates the difference between the predicted stage transition moments and the ground truth, which can be formulated as follows:

$$\mathcal{L}_{ce} = \sum_{i=1}^{\mathbb{K}} \text{CE}(a_i, \hat{a}_i), \quad (7)$$

where a_i represents the ground truth of the stage transition label.

D. Multi-Modal Fusion Module

To integrate the visual spatiotemporal feature F_{dy} and the hierarchical skeletal feature F_{sk} together, we propose a novel multi-modal fusion module, as illustrated in Figure 4. The attention map from F_{sk} is added to the map of F_{dy} to enhance the model’s ability to capture and understand human poses, ensuring accurate comprehension of target features across different perspectives or pose variations.

Specifically, the details of the fusion module are formulated in Equations 8 and 9. First, the i -th stage skeletal features F_{sk}^i and visual features F_{dy}^i within the \mathbb{K} stages are fed into individual linear layers to yield the queries Q^i , keys K^i , and values V^i with the same dimensions. The attention maps for the visual and skeletal features are then calculated separately and element-wise added to form a pose-guided attention map α^i . The pose-guided attention map is then multiplied by the value V^i to obtain the attention output $Atten^i$:

$$\alpha^i = \text{Softmax} \left(\frac{K_{dy}^i \cdot Q_{dy}^i}{\sqrt{D_{dy}}} + \rho \frac{K_{sk}^i \cdot Q_{sk}^i}{\sqrt{D_{pose}}} \right), \quad (8)$$

$$Atten^i = \text{Multihead}(V_{dy}^i \cdot \alpha^i). \quad (9)$$

where ρ represents a learnable weight parameter, D_{dy} and D_{pose} are the dimension values of the corresponding features, $i \in [1, \mathbb{K}]$. The whole formulation of the multi-modal fusion can be expressed as follows:

$$H_{dy} = Atten^i + LN(F_{dy}^i), \quad (10)$$

$$F_{fu}^i = FFN(LN(H_{dy})) + H_{dy}, \quad (11)$$

where LN and FFN denote Layer Normalization and Feed Forward Network, respectively.

E. Multi-stage Contrastive Regression Module

Stage-wise Contrastive Loss: After obtaining the segmented fused features F_{fu} and static features F_{st} , we introduce a stage-wise contrastive loss, denoted as \mathcal{L}_{cont} , to further enhance the differentiation between sub-actions at various stages. We

apply the stage-wise contrastive loss to F_{fu} and F_{st} separately, denoted as F in the following for simplification.

Formally, we define a critic function $sim(F^{(q,k)}, F^{(e,k)})$, where cos denotes cosine similarity, and $norm$ denotes a normalization function designed to enhance the critic’s expressive capacity, as follows:

$$\delta(F^{(q,k)}, F^{(e,k)}) = \cos(norm(F^{(q,k)}), norm(F^{(e,k)})). \quad (12)$$

During the calculation of the contrastive loss, we treat the features of the same stage in both the query video and the sample video as positive pairs, denoted as $\epsilon(F^{(q,k)}, F^{(e,k)})$. While negative pairs $\zeta(F^{(q,k)}, F^{(e,k)})$ can be divided into inter-video or intra-video pairs. Inter-video negative pair $(F^{(q,k)}, F^{(e,l)})$ consists of features from different stages in different videos, while intra-video pair $(F^{(q,k)}, F^{(q,l)})$ refers to features from different stages within the same video. The positive pairs $\epsilon(F^{(q,k)}, F^{(e,k)})$ and negative pairs $\zeta(F^{(q,k)}, F^{(e,k)})$ can be formulated as follows:

$$\epsilon(F^{(q,k)}, F^{(e,k)}) = e^{\delta(F^{(q,k)}, F^{(e,k)})/\tau}, \quad (13)$$

$$\zeta(F^{(q,k)}, F^{(e,k)}) = \sum_{k=1; k \neq l}^{\mathbb{K}} \left(\underbrace{e^{-\frac{\delta(F^{(q,k)}, F^{(e,l)})}{\tau}}}_{\text{inter negative pairs}} + \underbrace{e^{-\frac{\delta(F^{(q,k)}, F^{(q,l)})}{\tau}}}_{\text{intra negative pairs}} \right), \quad (14)$$

where τ denotes the temperature parameter and we set as 0.5 in practice. We define the pairwise objective for pair $(F^{(q,k)}, F^{(e,k)})$ considering the positive and negative terms as:

$$\ell(F^{(q,k)}, F^{(e,k)}) = \log \frac{\epsilon(F^{(q,k)}, F^{(e,k)})}{\epsilon(F^{(q,k)}, F^{(e,k)}) + \zeta(F^{(q,k)}, F^{(q,k)})}. \quad (15)$$

The stage contrastive loss is defined as the average over all given video pairs, denoted as \mathcal{L}_{cont} , formulated as follows:

$$\mathcal{L}_{cont} = \frac{1}{2\mathbb{K}} \sum_{i=1}^{\mathbb{K}} \left[\ell(F^{(q,k)}, F^{(e,k)}) + \ell(F^{(e,k)}, F^{(q,k)}) \right]. \quad (16)$$

Score Regression: We leverage the powerful representation capability of the Transformer to capture differences between the query pairs and the exemplar pairs across different stages. Specifically, we utilize a Transformer decoder \mathcal{D} to calculate the differences between the query and exemplar features for the k -th stage:

$$f_{fu}^k = \mathcal{D}(F_{fu}^{(q,k)}, F_{fu}^{(e,k)}), \quad (17)$$

$$f_{st}^k = \mathcal{D}(F_{st}^{(q,k)}, F_{st}^{(e,k)}), \quad (18)$$

where \mathcal{D} in both branches shares the same structure but different parameters, f_{fu}^k and f_{st}^k represent fusion and static difference features, respectively. In each block of \mathcal{D} , cross-attention is adopted to calculate the differences between query $F^{(q,k)}$ and exemplar $F^{(e,k)}$. $F_{fu}^{(q,k)}$ refers to the fusion feature of the k -th stage of the query video.

Finally, based on the generated difference fusion and static features, the stage contrastive regression network quantifies the action score difference between the query and exemplar

videos by learning relative scores. The predicted score \hat{S}^q for the query video V^q is calculated based on the exemplar video V^e as follows:

$$\hat{S}^q = S^e + \mathcal{CR}(F_{fu}, F_{st}), \quad (19)$$

$$\mathcal{CR}(F_{fu}, F_{st}) = \sum_{k=1}^{\mathbb{K}} \lambda_k (\mathcal{M}_{fu}(f_{fu}^k) + \mathcal{M}_{st}(f_{st}^k)), \quad (20)$$

where $F_{fu} = [f_{fu}^1, \dots, f_{fu}^{\mathbb{K}}]$ and $F_{st} = [f_{st}^1, \dots, f_{st}^{\mathbb{K}}]$, \mathcal{CR} denotes the stage-wise contrastive regression, which calculates the relative score difference between query video and exemplar video. This module incorporates two multi-layer perceptrons (MLPs) with ReLU activation, denoted as \mathcal{M}_{fu} and \mathcal{M}_{st} respectively. λ_k is a learnable weight parameter for different stages, which is normalized to ensure the contributions of the various stages are appropriately balanced. S^e is the actual score of the exemplar video, and \mathbb{K} is the number of stages.

To evaluate the accuracy of score prediction in the AQA task, we utilize the Mean Squared Error (MSE) as a metric. The MSE calculates the squared difference between the predicted scores and the ground truth values as the following:

$$\mathcal{L}_{aqa} = \text{MSE}(S^q, \hat{S}^q), \quad (21)$$

$$\text{MSE} = \frac{1}{N} \sum_{i=1}^N (y_i - \hat{y}_i)^2, \quad (22)$$

where N is the number of samples, y_i is the true value of the i -th sample, and \hat{y}_i is the predicted value.

F. Optimization and Inference

Optimization. For each video pair in the training data with pose sequences and score label S^q , the overall objective function for our task can be written as:

$$\mathcal{L} = \mathcal{L}_{aqa} + \mathcal{L}_{ce} + \mathcal{L}_{cont}. \quad (23)$$

Inference. For the query video V^q and the corresponding skeletal pose P^q in the test set, we adopt a multi-sample voting strategy to select N samples from the training set, obtaining the corresponding exemplar videos $\{V_i^e\}_{i=1}^N$ and exemplar skeletal pose $\{P_i^e\}_{i=1}^N$. We take $\{(V^q, P^q, V_i^e, P_i^e)\}_{i=1}^N$ as inputs, with their corresponding scores $\{S_i^e\}_{i=1}^N$. The inference process can be formulated as follows:

$$\hat{S}^q = \frac{1}{N} \sum_{i=1}^N (\mathcal{F}(V^q, P^q, V_i^e, P_i^e | \Theta) + S_i^e). \quad (24)$$

IV. FINEDIVING-POSE DATASET

To enable studies on fine-grained articulated action, we construct a new dataset termed FINEDIVING-POSE, which includes fully-annotated human skeletal pose labels.

A. Data Source

The widely-adopted FineDiving Dataset [14] and MTL-AQA Dataset [6] both lack human pose labels. The FineDiving Dataset contains 52 different diving categories, which substantially overlap with the categories present in the MTL-AQA Dataset. Therefore, we source data from the FineDiving dataset [14] and annotate all samples in FineDiving. A total of 367 videos and 12,722 frames are manually labeled to extract paired 2D human pose keypoints and bounding box labels according to the raw resolution, without any cropping or scaling. Additionally, using an automated annotation method, we label 3,000 videos and 288,000 frames, each accompanied by annotated 2D keypoints and bounding box labels, with 96 frames per video.

B. Annotation Pipeline

Most of the related work only employs HRNet [45] to estimate the human pose keypoints and present suboptimal performance, which are attributed to the following limitations: 1) The videos depict complex diving actions of the athletes, and HRNet struggles to estimate the precise human pose, due to the poor image quality resulting from high-speed motions and extreme body distortions. 2) The presence of both athletes and spectators within the frame often results in the model incorrectly estimating the pose of the audience members. To address these limitations, we implement a new annotation pipeline that integrates both manual and automatic annotation methodologies. The details are presented as follows:

Collection of manual annotated labels. To address the issue of blurred RGB images, we initially implement a series of data preprocessing steps to enhance the quality of the data and then manually annotate the skeletal keypoints. Specifically, we perform the cleaning of the dataset by removing synchronized diving videos and retaining 2,303 individual diving videos. We extract up to 10 videos per action number, based on 48 distinct diving action numbers, resulting in a total of 367 videos. The specific distribution of diving action numbers is provided in the supplementary material. We then extract the airborne movements of the divers across these videos, manually annotating each frame to construct the annotated dataset, which consists of 12,722 manually labeled images. These images encompass various poses, such as pike, tuck, and twist, with a resolution of 455×256 pixels for each image.

We utilize the LabelMe [46] tool for annotation and verification. The annotations adhere to the MPII data standard [47], encompassing the bounding box of the athlete and 16 pose keypoints. The bounding box is rectangular, with the top-left and bottom-right coordinates clearly annotated. The keypoints are represented as points, with the coordinates of their centers marked from 0 to 15. After the first round of annotation, the labels from one annotator are reviewed and refined by another annotator to ensure that each image contains annotations for both the bounding box and all 16 keypoints. Additional details about the keypoints and manual annotation process are provided in the supplementary material.

Collection of automatic annotated labels. The 12,722 annotated images serve as the training set to finetune the

HRNet. This process builds an athlete pose estimation network that achieves multi-scale fusion by exchanging information across parallel multi-resolution sub-networks. The network is responsible for resolving blurry images and extreme body distortions, thereby enabling more accurate estimation of highly contorted human poses. Prior to performing pose recognition, we propose to detect human targets in the image, locating all bounding boxes, and then using the pose estimator to detect keypoints within those bounding boxes. For target tracking, we opt for a simple yet effective method: the nearest neighbor algorithm, rather than using deep learning-based approaches. The primary rationale behind this choice is that in extreme pose scenarios, such as diving, the variation in human pose distribution is significant. Additionally, interference from spectators, referees, and other normal human poses complicates the task of tracking divers effectively using deep learning methods.

Specifically, given the athlete coordinates in the k -th frame are $p_k = (x_1, y_1, x_2, y_2)_k$, and the potential human coordinates in the next frame are $(x_1^i, y_1^i, x_2^i, y_2^i)_{k+1}$, where i represents the potential human target, then we calculate the distance between the i -th detected bounding box in the $k+1$ -th frame and other confirmed bounding boxes as follows:

$$dis_{k+1}^i = \sqrt{\sum_{j=1}^2 ((x_j^i - x_j)^2 + (y_j^i - y_j)^2)}. \quad (25)$$

Afterwards, we determine the final subject based on the confidence score and distance among human bounding boxes. Then, we adopt HRNet to obtain the more accurate athlete poses estimation based on the subject's coordinates, as the following:

$$P^q = \text{HRNet}\left(\left\{V_{(x_1, y_1, x_2, y_2)_k}^q\right\}_{k=1}^T\right), \quad (26)$$

where $\{V_k\}_{k=1}^T$ denotes the cropped images from frame 1 to frame T . Finally, for skeletal frames with incomplete joint sequences, joint interpolation is applied to reconstruct missing information. The interpolation formula is listed as follows:

$$p_k = p_i \frac{k-i}{j-i} + p_j \frac{j-k}{j-i}, \quad (27)$$

where p_i and p_j represent the coordinates of the corresponding skeletal nodes, and i, j are the i -th and j -th frames respectively.

C. Visualization Analysis of Annotated Data

Figure 5 shows the visualized differences between our introduced data annotations and the skeletal poses annotated by HRNet. We show various actions in the visualizations to demonstrate the effectiveness of our approach. For actions such as '407C' and '307C', we observe that for simpler actions (e.g., takeoff and final entry into the water), HRNet mostly identifies them correctly. However, during extreme poses, when there are multiple normal poses in the frame (e.g., referees and spectators), the model tends to focus more on the normally posed individuals. Furthermore, due to the twisted nature of human motion in extreme poses, the high-speed blurry video conditions further degrade the model's

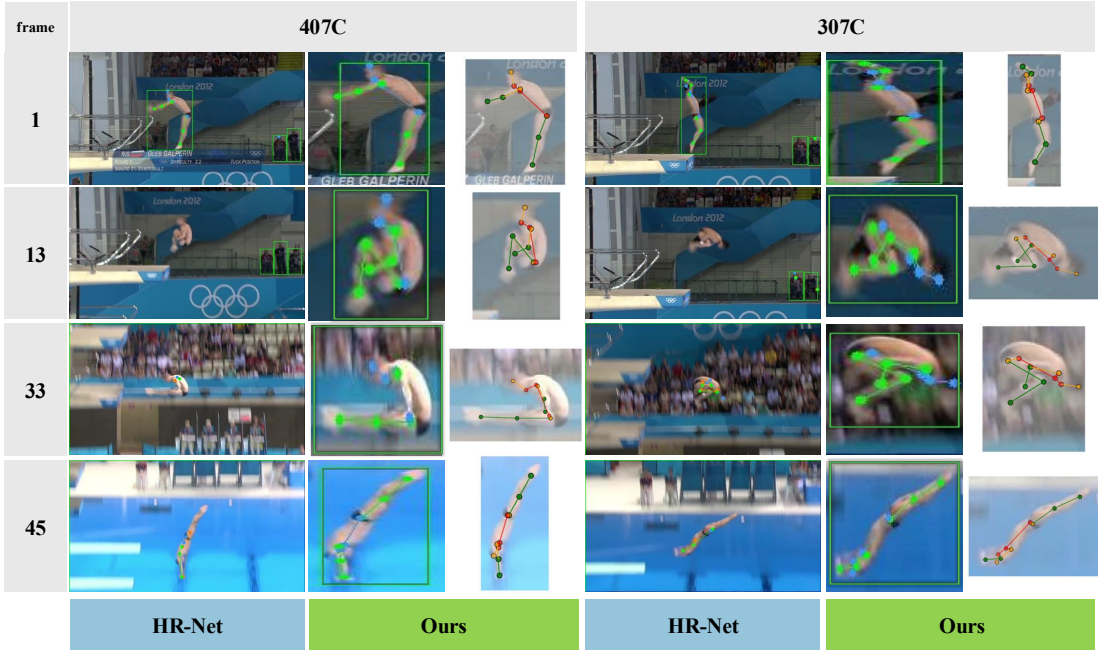


Fig. 5. Visualization examples of skeletons extracted using HRNet versus our proposed annotated method in FineDiving-Pose Dataset. In the first column of ‘407C’ and ‘307C’, we show the visualization results using HRNet, while the second and third columns present the visualization results using our method and the corresponding skeleton visualizations, respectively. Compared to the standard HRNet method, our proposed annotated method performs significantly better under extreme poses (e.g., flight and rotation) and effectively captures the athletes’ extreme poses.

performance. In contrast, our proposed annotated method (as shown in the second and third columns of ‘407C’) can effectively identify the athlete’s pose even under high-speed blur.

V. EXPERIMENT

In this section, we detail the experimental settings and present the results of our evaluations. We evaluate our proposed approach on two widely-adopted AQA datasets, i.e., *FineDiving* [14] and *MTL-AQA* [6].

A. Experiment Settings

FineDiving Dataset [14] comprises 3000 video samples, encompassing 52 dive numbers, 29 sub-action numbers, and 23 difficulty degree types. It provides exhaustive annotations, encompassing dive numbers (DN), sub-action numbers, coarse- and fine-grained temporal boundaries, as well as action scores-features. Here, DN refers to the action type labels, indicative of the specific sequence and categories of movements during a dive. Take DN ‘407C’ as an example, the first digit 4, represents an inward dive, the third digit 7, denotes the number of half somersaults to be completed, and ‘C’ signifies the tuck position. In this paper, the dataset is divided into 2,250 training samples and 750 test samples.

MTL-AQA Dataset [6] contains 1,412 fine-grained samples from 16 different events, captured from various perspectives. It provides different types of annotations to support research on multiple tasks, including action quality assessment, action recognition, and commentary generation. Additionally, it includes original score annotations from seven judges and the degree of difficulty (DD) for each action. In this paper, the dataset is divided into 1,059 training samples and 353 test samples.

Evaluation Metrics. Following [1], [2], [48], we use Spearman’s rank correlation coefficient (SRCC) to quantify the rank correlation between the true scores and predicted scores. A higher SRCC indicates a stronger scoring capability of the model. The computation of SRCC can be expressed as follows:

$$\rho = \frac{\sum_i (r_i - \bar{r})(\hat{r}_i - \bar{\hat{r}})}{\sqrt{\sum_i (r_i - \bar{r})^2 \sum_i (\hat{r}_i - \bar{\hat{r}})^2}}, \quad (28)$$

where r and \hat{r} represent the ranking for each sample of two series respectively. We also employ Relative L2-distance ($R_{\mathcal{L}_2}$) as an evaluation metric. $R_{\mathcal{L}_2}$ can be defined as follows:

$$R_{\mathcal{L}_2} = \frac{1}{N} \sum_{i=1}^N \left(\frac{|y_i - \hat{y}_i|}{y_{max} - y_{min}} \right). \quad (29)$$

Here, y_i and \hat{y}_i represent the ground truth and predicted scores for the i -th sample, respectively. Lower $R_{\mathcal{L}_2}$ indicates better performance of the approach. The computation of SRCC and $R_{\mathcal{L}_2}$ metrics in detail can be found in the paper [2].

Afterwards, we obtain the one-dimensional boundary box for each stage $[\hat{t}_{k-1}, \hat{t}_k]_{k=1}^{K-1}$. Assuming the ground truth boundary box denoted as $[t_{k-1}, t_k]_{k=1}^{K-1}$, we calculate the average Intersection over Union (IoU) between the predicted and ground truth boundary boxes. A prediction is considered correct if the IoU exceeds a certain threshold d . Thus, $\text{AIoU}@d$ is calculated as follows:

$$\text{AIoU}@d = \frac{1}{N} \sum_{i=1}^N \mathcal{J}(\text{IoU}_i \geq d), \quad (30)$$

where N is the number of samples. If the judgment is true, $\mathcal{J} = 1$, otherwise, $\mathcal{J} = 0$. In this work, we primarily adopt $\text{AIoU}@0.5$ and $\text{AIoU}@0.75$ as the main metrics.

TABLE I

COMPARISON RESULTS WITH THE STATE-OF-THE-ART METHODS ON FINEDIVING DATASET. BEST RESULTS ARE IN BOLD. HERE W/DN AND W/O DN REFER TO WITH AND WITHOUT USING DIVE NUMBERS.

Methods (w/o DN)	Year	ρ	$R_{\mathcal{L}_2}(\times 100)$	AIoU 0.5/0.75
USDL [4]	2020	0.8302	0.592	-
MUSDL [4]	2020	0.8427	0.573	-
CoRe [2]	2021	0.8631	0.556	-
TSA [14]	2022	0.8925	0.478	80.71 / 30.17
MCoRe [19]	2024	0.8897	0.461	89.42 / 74.46
Ours	2024	0.9041	0.411	98.17 / 93.68
Methods (w/ DN)	Year	ρ	$R_{\mathcal{L}_2}(\times 100)$	AIoU 0.5/0.75
USDL [4]	2020	0.8504	0.583	-
MUSDL [4]	2020	0.8978	0.370	-
CoRe [2]	2021	0.9061	0.361	-
TSA [14]	2022	0.9203	0.342	82.51 / 34.31
MCoRe [19]	2024	0.9232	0.326	98.26 / 79.17
Ours	2024	0.9365	0.244	99.46 / 97.18

Baseline Methods. We compare our method with the following approaches including Pose+DCT [3], C3D-LSTM [1], MUSDL [4], CoRe [2], TSA [14], TSA-Net [38], H-GCN [16], and MCoRe [19]. We adopt the publicly available code repositories to reproduce CoRe [2] and H-GCN [16] according to the parameter settings in the original papers, and we denote these results with an asterisk (*). For other methods, we cite the results reported in the original papers.

Implementation Details. We implemented our proposed method using PyTorch deep learning framework. The I3D model [35] pre-trained on the Kinetics dataset was utilized as the dynamic visual encoder. This encoder comprises the spatiotemporal feature extraction module and the mixed convolution module. The HD-GCN model [24] was adopted as the base model for the hierarchical skeletal encoder. In the multimodal fusion Transformer, the number of attention heads was set to 2. Additionally, the static visual encoder uses ResNet-50 [42] as the base model. The stage-wise decoder uses a multi-head attention network to calculate differences between various stages, with 4 heads used during training. The initial learning rate for the aforementioned models was set to $1e-3$, and the Adam optimizer was used with zero weight decay. Our model was trained with a batch size of 8 for 200 epochs. Following [14], we extracted 96 frames from each video in the FineDiving dataset and divided them into 9 clips in I3D. In the experiments on the MTL-AQA dataset, we extracted 103 frames per video clip following [2], and segmented them into 10 overlapping segments, each containing 16 consecutive frames. During inference, we sampled 10 exemplar videos for each query video, and aggregated their scores using a multi-sample voting strategy. We set the number of stage transitions \mathbb{K} as 3 according to the different stages of diving (*i.e.*, take-off, flying and entry).

B. Quantitative Results

We compare our proposed method against other AQA methods on FineDiving [14] and MTL-AQA [6] datasets. The results for FineDiving dataset are shown in Table I, while

TABLE II

COMPARISON RESULTS WITH THE STATE-OF-THE-ART METHODS ON MTL-AQA DATASET. BEST RESULTS ARE IN BOLD. HERE W/DD AND W/O DD REFER TO WITH AND WITHOUT DEGREE OF DIFFICULTY LABELS.

Approaches (w/o DD)	Year	ρ	$R_{\mathcal{L}_2}(\times 100)$
Pose+DCT [3]	2014	0.2682	-
C3D-SVR [1]	2017	0.7716	-
C3D-LSTM [1]	2017	0.8489	-
USDL [4]	2020	0.9066	0.654
MUSDL [4]	2020	0.9158	0.609
CoRe* [2]	2021	0.9223	0.466
H-GCN* [16]	2023	0.9178	0.487
Ours	2024	0.9266	0.446
Approaches (w/ DD)	Year	ρ	$R_{\mathcal{L}_2}(\times 100)$
USDL [4]	2020	0.9231	0.468
MUSDL [4]	2020	0.9273	0.451
CoRe* [2]	2021	0.9423	0.336
TSA-Net [38]	2021	0.9422	-
H-GCN* [16]	2023	0.9463	0.311
Ours	2024	0.9432	0.351

TABLE III

EVALUATION ON COMPONENTS OF MULTI-SCALE VISUAL-SKELETAL ENCODER IN THE FINEDIVING DATASET.

Approaches	DVE	SVE	HSE	ρ	$R_{\mathcal{L}_2}(\times 100)$
DVE	✓	x	x	0.8914	0.4784
SVE	x	✓	x	0.9173	0.3945
HSE	x	x	✓	0.6847	0.9871
DVE+HSE	✓	x	✓	0.9271	0.3377
DVE+SVE	✓	✓	x	0.9318	0.2914
Ours Full	✓	✓	✓	0.9365	0.2442

those for the MTL-AQA dataset are shown in Table II. We can clearly observe that our method significantly improved the SRCC and the $R_{\mathcal{L}_2}$ compared to all other methods on FineDiving. Specifically, our method achieved an SRCC of 0.9041 and an $R_{\mathcal{L}_2}$ of 0.411 without using dive numbers. When dive numbers are incorporated, the SRCC improves to 0.9364 and the $R_{\mathcal{L}_2}$ reduces to 0.244. Unlike TSA [14], which uses coarse-grained I3D to segment sub-actions, we introduced a static visual module and hierarchical skeletal features to capture fine-grained differences between sub-actions. Compared to TSA [14], our method achieved improvements of 1.16% and 1.68% in SRCC under the two conditions, respectively, and improvements of 0.067 and 0.098 in $R_{\mathcal{L}_2}$. On the MTL-AQA dataset, we evaluate the contribution with and without the difficulty (DD) labels. As shown in Table II, our proposed method significantly outperforms other methods in the (w/o DD) setting, achieving an SRCC of 0.9266 and an $R_{\mathcal{L}_2}$ of 0.446. Compared to the classic CoRe [2] method, our approach improves the SRCC by 0.43% and the $R_{\mathcal{L}_2}$ by 0.02. When DD are incorporated, the degree of difficulty serves as the reference standard for the distribution learning of H-GCN [16], allowing it to better calibrate the predicted distribution. However, in the absence of DD labels, our approach significantly outperforms H-GCN, achieving an SRCC improvement of 0.88% and a notable $R_{\mathcal{L}_2}$ improvement of 0.041. Our approach exhibits stronger generalizability, as the hierarchical skeletal encoder effectively guides the model to learn differences between actions even without DD labels.

TABLE IV
EVALUATION ON EFFECTIVENESS OF HIERARCHICAL SKELETAL ENCODER
IN THE FINEDIVING DATASET.

Approaches	ρ	$R_{\mathcal{L}_2}(\times 100)$
w/ H_0	0.9316	0.2867
w/ H_1	0.9310	0.2891
w/ H_2	0.9324	0.2814
w/ $H_0 + H_1$	0.9334	0.2703
w/o <i>EdgeConv</i>	0.9337	0.2665
ours	0.9365	0.2442

TABLE V
EVALUATION ON THE NUMBER OF STAGE IN THE FINEDIVING DATASET

\mathbb{K}	ρ	$R_{\mathcal{L}_2}(\times 100)$
1	0.9247	0.3522
2	0.9328	0.2884
2*	0.9316	0.2944
3	0.9365	0.2442

C. Ablation Study

We conduct a series of ablation experiments on our proposed method using the FineDiving dataset.

Multi-scale Visual-Skeletal Encoder. We analyze the effectiveness of each component in our multi-scale visual-skeletal model, including the dynamic visual encoder (DVE), static visual encoder (SVE), and hierarchical skeletal encoder (HSE). In the experiments, the number of stages is set as $\mathbb{K} = 3$, the number of layers in the Transformer decoder is 4, and the number of attention heads is 2. We evaluate each component in the Multi-scale Visual-Skeleton Encoder (MVSE) and present the results in Table III. The results demonstrate that each component in the MVSE plays a crucial role. Specifically, incorporating the HSE enables the model to capture subtle differences between sub-actions, achieving a 3.57% improvement in SRCC compared to the baseline. Additionally, utilizing the HSE alone results in inferior performance, with an SRCC of only 0.6847. It is attributed to the absence of some crucial visual information, such as splash size, which is vital for accurately evaluating the quality of the diving action.

Hierarchical Skeletal Encoder. We primarily analyze the impact of different levels of skeletal joints on the model’s ability. Specifically, we separately input the sub-action features learned by three different skeletal topologies into the multi-modal fusion model to evaluate the effectiveness of each level. We also assess the impact of adding EdgeConv for semantic edge modeling. As shown in Table IV, the experimental results indicate that different skeletal topologies have varying effects on guiding the model to learn sub-actions. For example, H_2 , which is employed to capture the coordination level of the athlete’s body movements, significantly enhances the model’s assessment of movement quality compared to H_0 and H_1 . This is reflected by an SRCC improvement of 0.14% over the other two levels. Moreover, we explored the impact of semantic edges on improving the model’s performance. Even the combination of H_0 and H_1 brings improvements, our full model including three levels human pose still achieves the

TABLE VI
EVALUATION ON THE NETWORK OF PROCEDURE SEGMENTATION MODULE

Approaches	ρ	$R_{\mathcal{L}_2}(\times 100)$	AIoU 0.5/0.75
FC	0.9230	0.3178	88.17 / 71.51
TCN [49]	0.9136	0.3725	83.17 / 34.99
ASFormer [50]	0.9357	0.2672	99.13 / 89.71
Ours	0.9365	0.2442	99.46 / 97.18

TABLE VII
EVALUATION ON THE NUMBER OF TEMPORAL SAMPLES IN THE
FINEDIVING DATASET

T	ρ	$R_{\mathcal{L}_2}(\times 100)$
3	0.9353	0.2469
5	0.9365	0.2442
8	0.9330	0.2552
10	0.9357	0.2455

best. By removing the EdgeConv module, the result drops by 2.8%. This finding suggests that incorporating fully connected semantic information can enhance the model’s generalization ability.

Procedure Segmentation Module. In the procedure segmentation module, we focus on the impact of the number of divided actions or distinct sub-action stages. Taking diving as an example, an athlete’s action can be segmented into three stages: takeoff, flight, and entry. The goal of this segmentation is to enable reasonable and accurate finer-grained scoring. Specifically, we explore the results under different segmentation scenarios. When $\mathbb{K} = 2$, the model divides the action into two stages using a single segmentation point. This segmentation point either separates takeoff or entry (denoted with *) from the whole movement. As shown in Table V, segmenting the stages during the diving process facilitates the model’s learning of finer-grained sub-actions. Compared to $\mathbb{K} = 1$ or 2, our method achieves up to a maximum of 1.18% in SRCC. Additionally, we conduct ablation experiments on the various backbones of the procedure segmentation network. We compare three different action segmentation models, *i.e.*, ASFormer [50], TCN [49], and using only a fully connected layer. As shown in Table VI, compared to other methods, our proposed approach is based on Bi-GRU, which utilizes gated units to control the flow and retention of temporal information, thereby enhancing the model’s ability to remember long-term dependencies and achieving the best performance. Additionally, in order to evaluate the impact of the temporal sampling size T on stage segmentation, we conducted a series of experiments, with the results being summarized in Table VII. We can observe that when T is too small, it results in insufficient semantic information, negatively affecting model performance, when T is too large, the performance reaches saturation, while increasing the complexity of the model. When T equals 5, our proposed model achieves the best performance and hence obtain a good trade-off.

Discussion on Multi-Modal Fusion Methods. We evaluate the performance of various fusion methods for combining visual and skeletal features. Specifically, we test

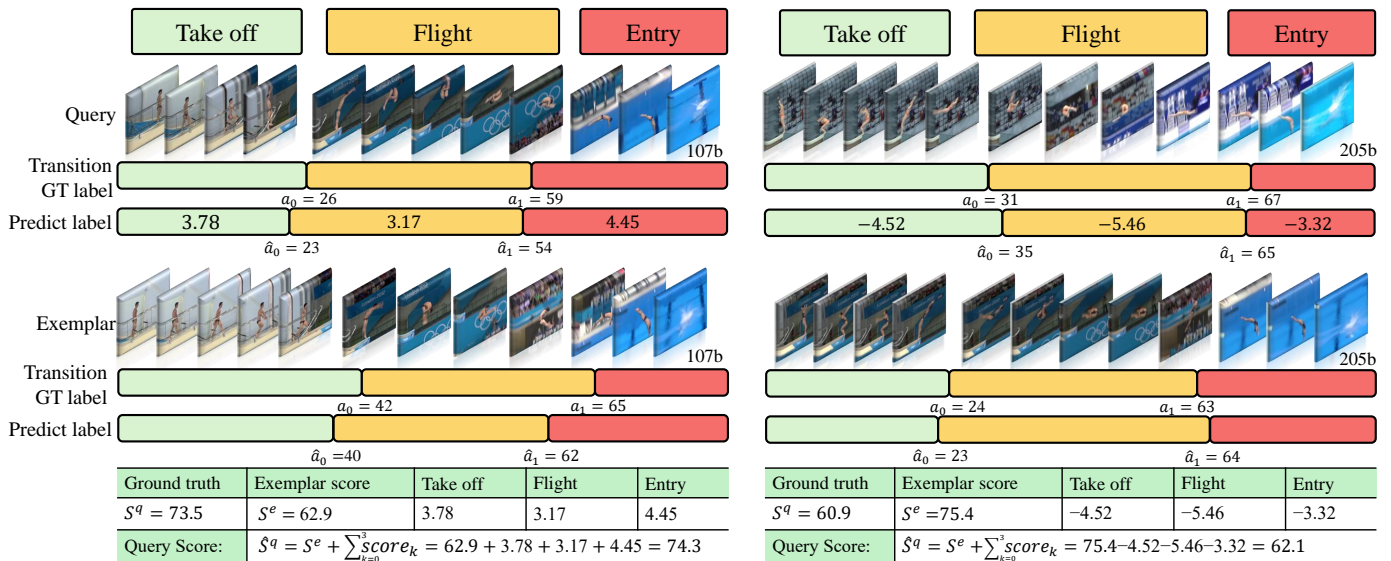


Fig. 6. Visualization of the predicted results. The input consists of a query video and an exemplar video. The videos are segmented into sub-actions, enabling stage predictions of relative scores for each sub-action. Subsequently, these relative scores are aggregated with the exemplar scores to compute the final predicted score.

TABLE VIII
EVALUATION ON THE LOSS OF CONTRASTIVE REGRESSION MODULE IN THE FINEDIVING DATASET

Loss	ρ	$R_{\mathcal{L}_2}(\times 100)$
InfoNCE Loss [51]	0.9142	0.3526
Triplet Loss [52]	0.9302	0.2962
Ours	0.9365	0.2442

TABLE IX
EVALUATION ON FUSION METHODS OF MFM IN THE FINEDIVING DATASET

Backbones	ρ	$R_{\mathcal{L}_2}(\times 100)$
Addition	0.9341	0.2874
Dot Product	0.9226	0.3189
Weighted Addition (Ours)	0.9365	0.2442

three approaches: Element-wise addition, Dot product, and our adopted Weighted addition. The experimental results are shown in Table IX. Compared to simple addition or multiplication of multimodal attention maps, our proposed method incorporates learnable fusion parameters to perform a weighted summation of visual and skeletal attention maps. Unlike the dot product, which often leads to attention sparsity, the weighted addition approach demonstrates superior representational capability, achieving a 1.39% improvement in SRCC results.

Stage-wise Contrastive Loss. In the multi-stage contrastive regression module, we evaluate the effectiveness of our proposed stage-wise contrastive loss by comparing it with two widely used contrastive losses: InfoNCE Loss [51] and Triplet Loss [52]. The experimental results are presented in Table VIII. Compared to InfoNCE, which relies on a large number of negative samples to ensure effective learning, our approach leverages both intra-video and inter-video negative samples

from multiple sources. This design enables our method to maintain effective learning with a significantly reduced number of contrastive samples. Compared to InfoNCE loss, our method achieves an improvement of 2.23% in SRCC.

D. Visualization Results

As illustrated in Figure 6, our proposed method begins by segmenting both the query and exemplar videos into sub-actions. In terms of diving, sub-actions are typically divided into three stages: ‘Takeoff’, ‘Flight’ and ‘Entry’. We can see from the figure that our proposed procedure segmentation module can accurately predict stage transition labels and effectively identify transitions between sub-actions. Subsequently, for each sub-action, our proposed multi-stage contrastive regression module can predict more accurate scores by comparing the query video with the exemplar video. For example, in the ‘Entry’ stage of ‘107b’ in Figure 6, the splash size in the query video is significantly smaller than that in the exemplar video. As a result, the relative score of the query video’s ‘Entry’ stage is noticeably higher than that of the exemplar video. Thus, the relative score for the ‘Entry’ stage of the query video is notably higher than that of the exemplar video. Finally, the relative scores of each sub-action are summed with the ground truth score S^e of the exemplar video to compute the predicted score \hat{S}^q for the query video. The predicted scores produced by our method exhibit a high degree of alignment with the ground truth, demonstrating the effectiveness of our approach.

VI. CONCLUSION

In this paper, we presented a hierarchically pose-guided multi-stage action quality assessment framework, of which a multi-scale visual-skeletal encoder was designed to capture features and physical priors from different modalities, and

a procedure segmentation network was proposed to segment sub-actions in videos. Furthermore, we leveraged a multi-stage contrastive learning regression to learn discriminative representations and achieved final evaluations. We demonstrated the effectiveness and superiority of the proposed method through extensive comparative and ablation experiments on two challenging AQA datasets and our newly-annotated FineDiving-Pose Dataset. In the future, we will extend the proposed model to automatic sports video captioning and tactics analysis.

REFERENCES

- [1] J. Pan, J. Gao, and W. Zheng, "Action assessment by joint relation graphs," in *Proc. IEEE Conf. Comput. Vis. Pattern Recognit.*, 2019, pp. 6331–6340.
- [2] X. Yu, Y. Rao, W. Zhao, J. Lu, and J. Zhou, "Group-aware contrastive regression for action quality assessment," in *Proc. IEEE Int. Conf. Comput. Vis.*, 2021, pp. 7919–7928.
- [3] H. Pirsiavash, C. Vondrick, and A. Torralba, "Assessing the quality of actions," in *Proc. Eur. Conf. Comput. Vis.*, 2014, pp. 556–571.
- [4] Y. Tang, Z. Ni, J. Zhou, D. Zhang, J. Lu, Y. Wu, and J. Zhou, "Uncertainty-aware score distribution learning for action quality assessment," in *Proc. IEEE Conf. Comput. Vis. Pattern Recognit.*, 2020, pp. 9839–9848.
- [5] Y. Bai, D. Zhou, S. Zhang, J. Wang, E. Ding, Y. Guan, Y. Long, and J. Wang, "Action quality assessment with temporal parsing transformer," in *Proc. Eur. Conf. Comput. Vis.*, 2022, pp. 422–438.
- [6] P. Parmar and B. T. Morris, "What and how well you performed? a multitask learning approach to action quality assessment," in *Proc. IEEE Conf. Comput. Vis. Pattern Recognit.*, 2019, pp. 304–313.
- [7] D. Shao, Y. Zhao, B. Dai, and D. Lin, "Intra- and inter-action understanding via temporal action parsing," in *Proc. IEEE Conf. Comput. Vis. Pattern Recognit.*, 2020, pp. 730–739.
- [8] A. Zia, Y. Sharma, V. Bettadapura, E. L. Sarin, and I. Essa, "Video- and accelerometer-based motion analysis for automated surgical skills assessment," *Int. J. Comput. Assist. Radiol. Surg.*, vol. 13, no. 3, pp. 443–455, 2018.
- [9] P. Parmar and B. Morris, "Action quality assessment across multiple actions," in *Proc. IEEE Winter Conf. Appl. Comput. Vis.*, 2019, pp. 1468–1476.
- [10] C. Xu, Y. Fu, B. Zhang, Z. Chen, Y.-G. Jiang, and X. Xue, "Learning to score figure skating sport videos," *IEEE Trans. Circuits Syst. Video Technol.*, vol. 30, no. 12, pp. 4578–4590, 2019.
- [11] Q. Zhang and B. Li, "Relative hidden markov models for video-based evaluation of motion skills in surgical training," *IEEE Trans. Pattern Anal. Mach. Intell.*, vol. 37, no. 6, pp. 1206–1218, 2015.
- [12] Y. Sharma, V. Bettadapura, N. Hammerla, S. Mellor, R. McNaney, P. Olivier, S. Deshmukh, A. McCaskie, and I. Essa, "Video-based assessment of osats using sequential motion textures," in *Proc. 5th Workshop Modeling Monitoring Comput. Assisted Interventions*, 2014, pp. 31–40.
- [13] A. Zia, Y. Sharma, V. Bettadapura, E. L. Sarin, M. A. Clements, and I. Essa, "Automated assessment of surgical skills using frequency analysis," in *Proc. Int. Conf. Med. Image Comput. Comput.-Assist. Intervent.*, 2015, pp. 430–438.
- [14] J. Xu, Y. Rao, X. Yu, G. Chen, J. Zhou, and J. Lu, "Finediving: A fine-grained dataset for procedure-aware action quality assessment," in *Proc. IEEE Conf. Comput. Vis. Pattern Recognit.*, 2022, pp. 2949–2958.
- [15] M. Qi, Y. Wang, J. Qin, A. Li, J. Luo, and L. V. Gool, "Stagnet: An attentive semantic rnn for group activity and individual action recognition," *IEEE Trans. Circuits Syst. Video Technol.*, vol. 30, no. 2, pp. 549–565, 2019.
- [16] K. Zhou, Y. Ma, H. P. H. Shum, and X. Liang, "Hierarchical graph convolutional networks for action quality assessment," *IEEE Trans. Circuits Syst. Video Technol.*, vol. 33, no. 12, pp. 7749–7763, 2023.
- [17] M. Qi, Y. Wang, A. Li, and J. Luo, "Stc-gan: Spatio-temporally coupled generative adversarial networks for predictive scene parsing," *IEEE Trans. Image Process.*, vol. 29, pp. 5420–5430, 2020.
- [18] K. Gedamu, Y. Ji, Y. Yang, J. Shao, and H. T. Shen, "Fine-grained spatio-temporal parsing network for action quality assessment," *IEEE Trans. Image Process.*, vol. 32, pp. 6386–6400, 2023.
- [19] Q. An, M. Qi, and H. Ma, "Multi-stage contrastive regression for action quality assessment," in *Proc. IEEE Int. Conf. Acoust., Speech, Signal Process.*, 2024, pp. 4110–4114.
- [20] H. Zhang, Y. Yuan, V. Makoviychuk, Y. Guo, S. Fidler, X. B. Peng, and K. Fatahalian, "Learning physically simulated tennis skills from broadcast videos," *ACM Trans. Graph.*, vol. 42, no. 4, pp. 1–14, 2023.
- [21] M. Li, H.-B. Zhang, Q. Lei, Z. Fan, J. Liu, and J.-X. Du, "Pairwise contrastive learning network for action quality assessment," in *Proc. Eur. Conf. Comput. Vis.*, 2022, pp. 457–473.
- [22] M. Nekoui, F. O. T. Cruz, and L. Cheng, "Falcons: Fast learner-grader for contorted poses in sports," in *Proc. IEEE Conf. Comput. Vis. Pattern Recognit. Workshops*, 2020, pp. 900–901.
- [23] M. Qi, W. Li, Z. Yang, Y. Wang, and J. Luo, "Attentive relational networks for mapping images to scene graphs," in *Proc. IEEE Conf. Comput. Vis. Pattern Recognit.*, 2019, pp. 3957–3966.
- [24] J. Lee, M. Lee, D. Lee, and S. Lee, "Hierarchically decomposed graph convolutional networks for skeleton-based action recognition," in *Proc. IEEE Int. Conf. Comput. Vis.*, 2023, pp. 10444–10453.
- [25] C. Lv, S. Zhang, Y. Tian, M. Qi, and H. Ma, "Disentangled counterfactual learning for physical audiovisual commonsense reasoning," *Adv. Neural Inform. Process. Syst.*, vol. 36, pp. 1–13, 2024.
- [26] M. Nekoui, F. O. T. Cruz, and L. Cheng, "Eagle-eye: Extreme-pose action grader using detail bird's-eye view," in *Proc. IEEE Winter Conf. Appl. Comput. Vis.*, 2021, pp. 394–402.
- [27] L. A. Zeng, F. T. Hong, W. S. Zheng, Q. Z. Yu, W. Zeng, Y. W. Wang, and J. H. Lai, "Hybrid dynamic-static context-aware attention network for action assessment in long videos," in *Proc. 28th ACM Int. Conf. Multimedia*, 2020, pp. 2526–2534.
- [28] Z. Li, Y. Huang, M. Cai, and Y. Sato, "Manipulation-skill assessment from videos with spatial attention network," in *Proc. IEEE Int. Conf. Comput. Vis. Workshops*, 2019, pp. 4385–4395.
- [29] W. Yun, M. Qi, F. Peng, and H. Ma, "Semi-supervised teacher-reference-student architecture for action quality assessment," in *Proc. Eur. Conf. Comput. Vis.*, 2025, pp. 161–178.
- [30] H. Doughty, D. Damen, and W. Mayol-Cuevas, "Who's better? who's best? pairwise deep ranking for skill determination," in *Proc. IEEE Conf. Comput. Vis. Pattern Recognit.*, 2018, pp. 6057–6066.
- [31] M. Qi, J. Qin, Y. Yang, Y. Wang, and J. Luo, "Semantics-aware spatial-temporal binaries for cross-modal video retrieval," *IEEE Trans. Image Process.*, vol. 30, pp. 2989–3004, 2021.
- [32] H. Doughty, W. Mayol-Cuevas, and D. Damen, "The pros and cons: Rank-aware temporal attention for skill determination in long videos," in *Proc. IEEE Conf. Comput. Vis. Pattern Recognit.*, 2019, pp. 7862–7871.
- [33] J.-H. Pan, J. Gao, and W.-S. Zheng, "Adaptive action assessment," *IEEE Trans. Pattern Anal. Mach. Intell.*, vol. 44, no. 12, pp. 8779–8795, 2021.
- [34] D. Tran, L. Bourdev, R. Fergus, L. Torresani, and M. Paluri, "Learning spatiotemporal features with 3d convolutional networks," *IEEE*, 2015.
- [35] J. Carreira and A. Zisserman, "Quo vadis, action recognition? a new model and the kinetics dataset," in *Proc. IEEE Conf. Comput. Vis. Pattern Recognit.*, 2017, pp. 6299–6308.
- [36] P. Parmar and B. T. Morris, "Learning to score olympic events," in *Proc. IEEE Conf. Comput. Vis. Pattern Recognit. Workshops*, 2017, pp. 20–28.
- [37] X. Shi, Z. Chen, H. Wang, D.-Y. Yeung, W.-K. Wong, and W.-C. Woo, "Convolutional lstm network: A machine learning approach for precipitation nowcasting," in *Proc. Adv. Neural Inf. Process. Syst.*, 2015, pp. 802–810.
- [38] S. Wang, D. Yang, P. Zhai, C. Chen, and L. Zhang, "Tsa-net: Tube self-attention network for action quality assessment," in *Proc. 29th ACM Int. Conf. Multimedia*, 2021, pp. 4902–4910.
- [39] A. Ahmadi, D. Rowlands, and D. A. James, "Towards a wearable device for skill assessment and skill acquisition of a tennis player during the first serve," *Sports Technol.*, vol. 2, no. 3–4, pp. 129–136, 2009.
- [40] M. Bourgain, S. Hybois, P. Thoreux, O. Rouillon, P. Rouch, and C. Sauret, "Effect of shoulder model complexity in upper-body kinematics analysis of the golf swing," *J. Biomech.*, vol. 75, pp. 154–158, 2018.
- [41] L. Okamoto and P. Parmar, "Hierarchical neurosymbolic approach for comprehensive and explainable action quality assessment," in *Proc. IEEE Conf. Comput. Vis. Pattern Recognit.*, 2024, pp. 3204–3213.
- [42] K. He, X. Zhang, S. Ren, and J. Sun, "Deep residual learning for image recognition," in *Proc. IEEE Conf. Comput. Vis. Pattern Recognit.*, 2016, pp. 770–778.
- [43] Y. Wang, Y. Sun, Z. Liu, S. E. Sarma, M. M. Bronstein, and J. M. Solomon, "Dynamic graph cnn for learning on point clouds," *ACM Trans. Graph.*, 2019.
- [44] K. Cho, B. V. Merriënboer, C. Gulcehre, D. Bahdanau, F. Bougares, H. Schwenk, and Y. Bengio, "Learning phrase representations using rnn encoder-decoder for statistical machine translation," *arXiv:1406.1078*, 2014.

- [45] J. Wang, K. Sun, T. Cheng, B. Jiang, C. Deng, Y. Zhao, D. Liu, Y. Mu, M. Tan, X. Wang *et al.*, “Deep high-resolution representation learning for visual recognition,” *IEEE Trans. Pattern Anal. Mach. Intell.*, vol. 43, no. 10, pp. 3349–3364, 2020.
- [46] B. C. Russell, A. Torralba, K. P. Murphy, and W. T. Freeman, “Labelme: A database and web-based tool for image annotation,” *Int. J. Comput. Vis.*, vol. 77, pp. 157–173, 2008.
- [47] M. Andriluka, L. Pishchulin, P. Gehler, and B. Schiele, “2d human pose estimation: New benchmark and state of the art analysis,” in *Proc. IEEE Conf. Comput. Vis. Pattern Recognit.*, 2014, pp. 3686–3693.
- [48] J. Xu, S. Yin, G. Zhao, Z. Wang, and Y. Peng, “Fineparser: A fine-grained spatio-temporal action parser for human-centric action quality assessment,” in *Proc. IEEE Conf. Comput. Vis. Pattern Recognit.*, 2024, pp. 14 628–14 637.
- [49] S. Bai, J. Z. Kolter, and V. Koltun, “An empirical evaluation of generic convolutional and recurrent networks for sequence modeling,” 2018, arXiv:1803.01271.
- [50] F. Yi, H. Wen, and T. Jiang, “Asformer: Transformer for action segmentation,” in *Proc. Brit. Mach. Vis. Conf.*, 2021, pp. 1–15.
- [51] A. van den Oord, Y. Li, and O. Vinyals, “Representation learning with contrastive predictive coding,” 2018, arXiv:1807.03748.
- [52] M. Schultz and T. Joachims, “Learning a distance metric from relative comparisons,” *Adv. Neural Inf. Process. Syst.*, vol. 16, 2003.